PHYSICAL REVIEW B **100**, 064101 (2019)

Property control from polyhedral connectivity in ABO_3 oxides

Nicholas Wagner,[1] Ram Seshadri,[2] and James M. Rondinelli[1,*]
[1] *Department of Materials Science and Engineering, Northwestern University, Evanston, Illinois 60208, USA*
[2] *Materials Department and Materials Research Laboratory, University of California, Santa Barbara, California 93106, USA*

(Received 22 March 2019; revised manuscript received 2 July 2019; published 1 August 2019)

We investigate the effect of the degree of metal-oxygen octahedral facesharing on the mechanical and electronic properties of d^0 $BaTiO_3$ and d^3 $BaMnO_3$. We find that increased facesharing softens the elastic constants of both materials due to the increased volume per atom, with polar distortions also contributing to the reduction in the bulk modulus. Owing to orbital filling in the d manifold, we find the electronic band gap of $BaTiO_3$ is relatively unaffected by changes in percent facesharing whereas the band gap of $BaMnO_3$ increases by more than 200% as the percent facesharing increases from 0% (cubic perovskite) to 100% (hexagonal $BaNiO_3$ perovskite). We identify that the trigonal distortions present in the face-connected polymorphs represent useful atomistic structural knobs to tune band structure in hexagonal perovskites. Our results indicate that facesharing hexagonal polymorphs provide an expanded oxides arena with additional structural flexibility beyond the usual fully corner-connected perovskites for property control.

DOI: 10.1103/PhysRevB.100.064101

I. INTRODUCTION

The properties of complex oxides are sensitive to changes in the local and extended crystal structure because of the sensitivity of electron-, spin-, and orbital-lattice interactions to perturbations of metal-oxygen (B-O) bond lengths and metal-oxygen-metal (B-O-B) bond angles [1]. Consequently, a number of strategies are employed to direct the atomic structure towards achieving desired mechanical and electronic responses, e.g., in ABO_3 perovskite oxides that find use in photovoltaic [2], ferroelectric [3], oxygen evolution [4], and other applications. These approaches include using chemical pressure [5], cation size effects [6], and doping in bulk oxides. In addition, epitaxial strain [7,8], proximity and confinement effects [9–13], and substrate orientation (geometric lattice engineering) are used in heterostructures [14–17] and superlattices [18,19] of thin film oxides.

The aforementioned chemical and mechanical perturbations all preserve the BO_6 octahedral connectivity—the octahedra remain corner-connected in cubic perovskites with abc/abc cubic-close packing of AO_3 layers along [111]. Alternative octahedral connectivies, including edge- and facesharing, are found either alone or coexisting with corner-shared octahedra in many complex oxides [20]; however, the impacts of such connectivity differences on physical properties [21] and the dependencies with composition [22] are often less understood. These facts in part explain why connectivity remains to be exploited for property control. A glimpse of what is possible using a connectivity-control knob is evident from earlier reports of over 1-eV band gap variations with connectivity changes in the $AMnO_3$ (A = Ca, Sr, Ba) series [23].

Hexagonal perovskite oxides exhibit at least two BO_6 octahedra connected by a common face owing to ab/ab stacking of AO_3 layers. This stacking is generally found for tolerance factors [24] greater than 1, indicating geometric frustration of the cubic close packing. Hexagonal ABO_3 oxides with mixed abc and ab stacking of AO_3 layers exhibit crystal structures with proportions of face- and corner-shared octahedra decreasing from 100% (chainlike structures) to 0% (cubic perovskite) as shown in Fig. 1. Note that not all available hexagonal stackings are depicted. For example, $BaIrO_3$ and $BaRuO_3$ exhibit structures with 67% facesharing [25,26], while $BaMnO_3$ exhibits a wide variety of polytypes depending on synthesis conditions [27]. The former compounds are of recent interest because they exhibit metal-insulator [28] and ferromagnetic Mott insulator to paramagnetic charge-ordered insulator [25] transitions.

Although this change in facesharing percentage may appear as no more than a crystallographic curiosity, it alters the nature of the spin interactions and the onsite orbital energies. The nearest-neighbor antiferromagnetic or ferromagnetic superexchange interactions evolve as the proportion of 180° to ≈80° B-O-B bond angles and B-O bond lengths change, impacting the strength of the B d and O p orbital overlap, with different facesharing percentages.

In addition, the crystal field split d orbital energies of BO_6 octahedra sharing a common face differ from those of octahedra sharing only a corner [21]. Rather than the triply degenerate antibonding t_{2g} and doubly degenerate e_g^σ orbitals observed in a cubic perovskite, the t_{2g} orbital levels of the facesharing cation are further split by a trigonal distortion of the oxygen octahedra and additional electrostatic contributions from neighboring cations (Fig. 1, right). The splitting results in a single a_{1g} orbital similar to an atomic d_{z^2} orbital pointed along the [001] chain direction, and doubly degenerate e_g^π orbitals, which resemble two d_{xy} orbitals rotated on their sides and separated by 45° rotations about z. The e_g^σ

---

[*] jrondinelli@northwestern.edu

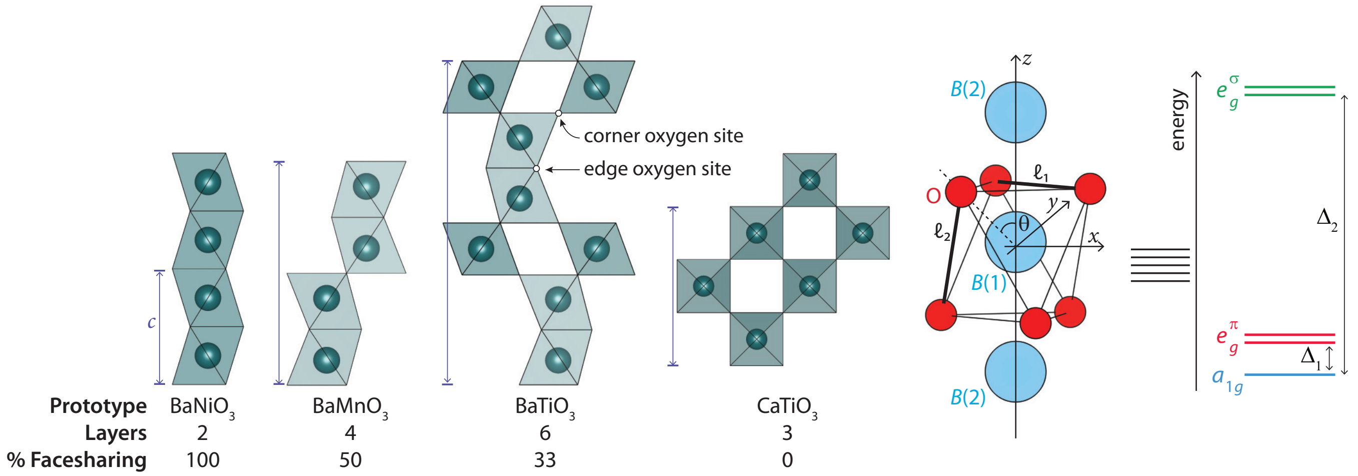

FIG. 1. Changes in octahedral connectivity and orbital structure in ABO$_3$ perovskites. Perovskites with different percentages of facesharing. (Right) Local coordination of a transition metal B cation in a trigonally distorted O$_6$ octahedron. An ideal undistorted octahedron with equal bond lengths exhibit a trigonal angular distortion $\theta = \arccos(1/\sqrt{3})$ and a trigonal octahedral strain $\eta = \ell_1/\ell_2 = 1$. Crystal field splitting of the degenerate $B(1)\,t_{2g}$ levels (Δ_1) is due to these trigonal distortions and the contribution from the neighboring $B(2)$ cations to the crystal field. The sign of Δ_1 reverses if the trigonal distortion is compressive rather than tensile as depicted here.

orbitals resemble atomic d_{z^2} and $d_{x^2-y^2}$ orbitals rotated by 45° about x to point along the metal-ligand bonds. It is the trigonal distortion permitted in perovskites with mixed *abc* and *ab* stacking that largely controls the energy differences between these bands and makes it possible to invert the occupied orbitals. Despite the diversity of hexagonal polymorphs, and thus the potential property variation accessible, they are less well-studied because of the limited number of chemistries with suitable tolerance factors under standard temperature and pressure conditions. Interestingly, when hexagonal phases are investigated, it is often because they are a deleterious phase that inhibit material performance, such as in ion transport [29].

Here we investigate the bulk moduli and electronic band gap dependencies on octahedral facesharing for d^0 BaTiO$_3$ ($t = 1.071$ [30]) and d^3 BaMnO$_3$ ($t = 1.113$ [30]) from both local ionic models of linear facesharing octahedral chains and density functional theory calculations that treat the electronic degrees of freedom with the full crystallography of the structures. We find a nonmonotonic dependence of the elastic response in both compounds; the stiffnesses of the materials increase as the percentage of facesharing octahedra increase, but then weakens for the 100% face sharing (hexagonal) polymorphs. The maximum mechanical stiffness for intermediate polyhedral-connectivity fractions arises from a trade-off between stiffening along the c direction as more octahedra are linked by faces with softening arising from a decrease in atomic density as the structures exhibit more faceshared octahedra. We also find increases in the electronic band gap by ≈1 eV as the percentage of facesharing increases for BaMnO$_3$, whereas the band gap of BaTiO$_3$ first decreases by ≈0.2 eV before returning to its nominal cubic perovskite value. These differences are attributed to the different d-band fillings for the titanate and managanate. For BaMnO$_3$, the conduction bandwidth narrows as the Mn-O-Mn bond angles decrease. The trigonal distortions in the lattice weakly modify the conduction band because it is formed from Mn e_g^π states. In contrast, the electronic band dispersions are weakly affected by the percentage facesharing in BaTiO$_3$; however, because the conduction band exhibits a_{1g} character, it is sensitive to the trigonal distortions that modify the Ti-Ti distances along the facesharing direction. We find that the trigonal distortions may be an effective structural degree-of-freedom for tuning band gaps in hexagonal perovskites, and it may be accessible using thin-film epitaxial growth methods. Our results indicate hexagonal phases offer added structural flexibility for tuning material properties in ways not directly accessibly to cubic perovskites.

II. COMPUTATIONAL METHODS

A. Ionic model

We compute the splitting of the d orbital manifold by the oxide ion within an octahedral crystal field with respect to the trigonal distortion using a point-charge approximation following the approach in Ref. [21]. The Hamiltonian is solved analytically using MATHEMATICA [31], and the notebook file is available in Refs. [32,33] . In this model, the wave functions corresponding to e_g^σ, e_g^π, and a_{1g} character and their eigenenergies depend upon θ, the trigonal angular distortion angle defined as the smallest angle between the B-O bonds and the neighboring B site as shown in Fig. 1. We also define the quantity η to be the trigonal octahedral strain as the ratio between the O-O distance of the ligands forming the triangular BO$_6$ face normal to z, ℓ_1 as shown in Fig. 1, relative to the O-O distance on an adjacent face, ℓ_2. For compressive (tensile) trigonal octahedral strains, this ratio is larger (less) than the ideal value of unity.

In addition, Table I provides the orbital definitions within the trigonal crystal field in terms of the atomic orbitals. Here we include metal-metal interactions within the model. Owing to the chemistries of interest here, we treat only tetravalent B^{4+} cations. An additional parameter, $\kappa = 0.1$, is used in all model calculations. It is a material constant that describes

TABLE I. Relationships among the d orbitals within an octahedral crystal field relative to those in a trigonal crystal field. The coordinate reference frame for the orbitals in the trigonal crystal field are defined such that the z axis is along the $3d$ cation chain as given in Fig. 1.

Octahedral field		Trigonal field	
Symmetry	Orbitals	Symmetry	Orbitals
t_{2g}	d_{xy}	a_{1g}	d_{z^2}
	d_{yz}	e_g^{π}	$-\frac{2}{\sqrt{6}}d_{xy}+\frac{2}{\sqrt{3}}d_{yz}$
	d_{xz}		$\frac{2}{\sqrt{6}}d_{x^2-y^2}+\frac{1}{\sqrt{3}}d_{xz}$
e_g	$d_{x^2-y^2}$	e_g^{σ}	$\frac{1}{\sqrt{3}}d_{x^2-y^2}-\sqrt{\frac{2}{3}}d_{xz}$
	d_{z^2}		$-\frac{1}{\sqrt{3}}d_{xy}-\sqrt{\frac{2}{3}}d_{yz}$

the strength of the crystal field and the radial part of the hydrogenic d-orbital wave functions [21].

B. Density functional theory

We perform density functional theory (DFT) calculations with the PBEsol exchange-correlation functional [34] as implemented in the Vienna *ab initio* simulation package (VASP). [35–37]. We used a 600-eV cutoff energy for the plane-wave basis in all variable-cell and atomic relaxations and electronic densities of states calculations. The projector augmented wave (PAW) pseudopotentials [38] are used with the following valence configurations: Ba: $5s^25p^66s^2$, Mn: $3p^64s^13d^6$, and Ti: $3p^64s^13d^3$, O: $2s^22p^4$.

Calculations on $BaMnO_3$ were performed without the plus Hubbard U correction [39], as our test calculations showed the manganate polymorphs did not require any special treatment of strong electron correlations to capture the insulating ground state, making them all band insulators. Likewise, our structures agree with experimental reports. The largest relative error in lattice parameters is 1.7%, while the largest error in bond lengths is 0.039 Å. All equilibrium $BaMnO_3$ structures exhibit G-type antiferromagnetic spin structures in our calculations where the spins of nearest neighbor Mn sites are antialigned in all three dimensions in agreement with experiments [40,41].

A greater 700-eV plane-wave cutoff was used to calculate the elastic constants. We sampled the Brillouin zone using an $8 \times 8 \times 8$ k-point mesh in all cases except for the 33% facesharing structure where an $8 \times 8 \times 6$ mesh was used due to the larger c lattice parameter. Elastic moduli were calculated with the strain-stress relationship method as implemented in VASP [42,43], and the bulk moduli are obtained using a Voigt average [44]. Maximally localized Wannier functions were constructed using WANNIER90 [45] with random initial projections.

III. RESULTS AND DISCUSSION

A. Structure and stability

We first compute the equilibrium crystal structure for $BaTiO_3$ and $BaMnO_3$ with varying percentage of facesharing octahedra. The DFT relaxed structures are given in Table II and the experimental structures are provided in Ref. [33]. Here we summarize the experimentally observed polymorphs: $BaMnO_3$ exhibits 100% facesharing when synthesized with weeks of heat treatment at 1000 °C followed by cooling to room temperature at 18 °C/h [40]. 50% facesharing $BaMnO_3$ is metastable at room temperature but can be prepared by first heating reactants at 1300 °C under argon before oxidizing at 600 °C [41]. $BaTiO_3$ with the 33% facesharing structure is also metastable at room temperature but can be prepared by quenching from above 1432 °C [46]. The orthorhombic 0% facesharing structure is stable between −90 °C and 5 °C [47].

We find that the titanate and manganate exhibit centrosymmetric crystal structures except for $BaTiO_3$ with 0% and 100% facesharing; in these metastable polymorphs, the Ti cations spontaneously off center along the [110] and [001] directions, respectively. In the 33% and 50% polymorphs of both $BaTiO_3$ and $BaMnO_3$, antipolar distortions are present along the [001] direction. $BaMnO_3$ in the 0% facesharing perovskite structure is also stabilized in the polar $Amm2$ space group. The various polar and antipolar distortions are schematically illustrated in Fig. 2. The calculated structures are in good agreement with reported structures obtained by x-ray and neutron diffraction (see Ref. [33]). The lattice parameters a, b, and c are slightly underestimated, but the differences ($<1.7\%$) are within standard errors of DFT with a semilocal exchange-correlation functional and the absence of treating finite temperature effects (thermal expansion). Similarly, the B-O bond lengths are at most 0.9% shorter. The 100% facesharing $BaMnO_3$ phase is known to undergo a displacive phase transition at 130 K to a structure exhibiting $P6_3mc$ symmetry [48], but the room temperature $P6_3/mmc$ structure is used here to simplify comparisons with $BaTiO_3$. The $P6_3mc$ phase is lower in free energy by approximately 4.5 meV per formula unit (f.u.) compared to the $P6_3/mmc$ structure. Ba is coordinated by 12 oxide anions in every structure except the polar 100% facesharing $BaTiO_3$, where it exhibits nine coordination. The transition metal B cation is always octahedrally coordinated.

Figure 3 shows the evolution in the bond lengths, trigonal octahedral strain η, and bond angles with percentage facesharing. With increasing BO_6 octahedral face connectivity, the overall trend is for the Ba-O distances to increase [panel (a)], while the B-O bond lengths shorten [panel (b)]. Interestingly, the average Ti-O bond length of the 100% facesharing $BaTiO_3$ polymorph is longer than the 50% facesharing polymorph. Its Ba-O bond distance is also shorter. We attribute this response to the cooperative polar Ti off-centering that is present in the 100% facesharing structure, which differs from the antipolar off-centering in the 50% facesharing structure (Fig. 2).

In hexagonal perovskites exhibiting some or all faceshared octahedra, the electrostatic repulsion between neighboring B cations imposes chemical stresses that lead to trigonal octahedral strain, manifesting as inequivalent O-O distances on the triangular O-O-O faces of the BO_6 units. Figure 3(c) shows that $BaTiO_3$ and $BaMnO_3$ accommodate this repulsion in a similar manner, despite the different transition metal orbital filling as seen by comparing η with percentage facesharing. Increasing the percentage of facesharing decreases η from unity to ≈0.9, which indicates the octahedra are

TABLE II. Crystallographic data for perovskite polymorphs of $BaTiO_3$ and $BaMnO_3$ obtained at the DFT-PBEsol level. Experimental structures, where available, are provided electronically in Ref. [33].

			$B = \mathrm{Ti}$					$B = \mathrm{Mn}$	
0% facesharing			$Amm2$ (No. 38) $a = 3.960$ Å, $b = 5.681$ Å, $c = 5.703$ Å $\alpha = \beta = \gamma = 90^\circ$					$Amm2$ (No. 38) $a = 3.851$ Å, $b = 5.537$ Å, $c = 5.573$ Å $\alpha = \beta = \gamma = 90^\circ$	
Atom	Site	x	y	z	Atom	Site	x	y	z
Ba	$2a$	0	0	0.00226	Ba	$2a$	0	0	0.00134
Ti	$2b$	0	1/2	0.51622	Mn	$2b$	1/2	0	0.48676
O(1)	$2a$	0	0	0.48707	O(1)	$2a$	0	0	0.50957
O(2)	$4e$	1/2	0.75513	0.73452	O(2)	$4e$	1/2	0.74352	0.76386
33% facesharing			$P6_3/mmc$ (No. 194) $a = b = 5.708$ Å, $c = 13.911$ Å $\alpha = \beta = 90^\circ,\ \gamma = 120^\circ$					$P6_3/mmc$ (No. 194) $a = b = 5.561$ Å, $c = 13.510$ Å $\alpha = \beta = 90^\circ,\ \gamma = 120^\circ$	
Atom	Site	x	y	z	Atom	Site	x	y	z
Ba(1)	$4f$	1/3	2/3	0.09685	Ba(1)	$4f$	1/3	2/3	0.58976
Ba(2)	$2b$	0	0	1/4	Ba(2)	$2b$	0	0	1/4
Ti(1)	$4f$	1/3	2/3	0.84622	Mn(1)	$4f$	1/3	2/3	0.34423
Ti(2)	$2a$	0	0	0	Mn(2)	$2a$	0	0	0
O(1)	$12k$	0.16524	0.33048	0.58058	O(1)	$12k$	0.16502	0.33004	0.08019
O(2)	$6h$	0.51707	0.03413	1/4	O(2)	$6h$	0.47881	−0.04238	1/4
50% facesharing			$P6_3/mmc$ (No. 194) $a = b = 5.734$ Å, $c = 9.433$ Å $\alpha = \beta = 90^\circ,\ \gamma = 120^\circ$					$P6_3/mmc$ (No. 194) $a = b = 5.594$ Å, $c = 9.119$ Å $\alpha = \beta = 90^\circ,\ \gamma = 120^\circ$	
Atom	Site	x	y	z	Atom	Site	x	y	z
Ba(1)	$2a$	0	0	0	Ba(1)	$2a$	0	0	0
Ba(2)	$2d$	1/3	2/3	3/4	Ba(2)	$2d$	1/3	2/3	3/4
Ti	$4f$	1/3	2/3	0.11139	Mn	$4f$	1/3	2/3	0.11206
O(1)	$6g$	1/2	0	0	O(1)	$6g$	1/2	0	0
O(2)	$6h$	0.18406	0.36811	1/4	O(2)	$6h$	0.18719	0.37438	1/4
100% facesharing			$P6_3mc$ (No. 186) $a = b = 5.775$ Å, $c = 5.110$ Å $\alpha = \beta = 90^\circ,\ \gamma = 120^\circ$					$P6_3/mmc$ (No. 194) $a = b = 5.667$ Å, $c = 4.734$ Å $\alpha = \beta = 90^\circ,\ \gamma = 120^\circ$	
Atom	Site	x	y	z	Atom	Site	x	y	z
Ba	$2b$	1/3	2/3	0.29736	Ba	$2c$	1/3	2/3	1/4
Ti	$2a$	0	0	0.50478	Mn	$2a$	0	0	0
O	$6c$	0.84871	0.15129	0.21679	O	$6h$	0.85022	0.70045	1/4

stretched along c as the oxide anions forming an octahedral face normal to z are brought closer together. Although η for both $BaMnO_3$ and $BaMnO_3$ quickly decrease from the cubic perovskite values as the structure adopts a finite fraction of facesharing, the qualitative dependencies with increasing percentage of facesharing are different. $BaTiO_3$ exhibits essentially a monotonically decreasing trend with the 100% $BaTiO_3$ polymorph exhibiting a larger trigonal distortion than the 50% facesharing structure. This behavior is due likely to the cooperative polar Ti displacements along the c axis, which lead to further compression of the triangular O-O-O face as the oxide anions displace to screen the enhanced Ti-Ti repulsion [49]. A similar, much weaker effect is seen in rhombohedral $BaTiO_3$ where $\eta = 0.98$. While the O move closer together in the O-O-O face normal to the polar axis, they are only screening the weaker Ti-Ba repulsion. This behavior is not found in the manganate. The 100% facesharing $BaMnO_3$ structure has more regular octahedra than the 33% and 50% structures because the antipolar distortion of the Mn is absent. Figures 3(d) and 3(e) show the minimum M-O-M bond angles shrink quickly from ≈170° to 84° upon the shift from 0 to 33% facesharing due to the change in bonding pattern before slightly declining further to ≈80°. For the intermediate facesharing structures, the B-O-B angles between octahedra connected by corners increase from the value seen in the orthorhombic 0% structure. As the bonds between corner-connected octahedra straighten with increased percentage facesharing, the bond angles between faces decrease and are brought closer together.

Figure 4 shows the phase stability for $BaTiO_3$ and $BaMnO_3$ with varying percentage of facesharing octahedra, where 0% indicates a fully corner-connected orthorhombic symmetry

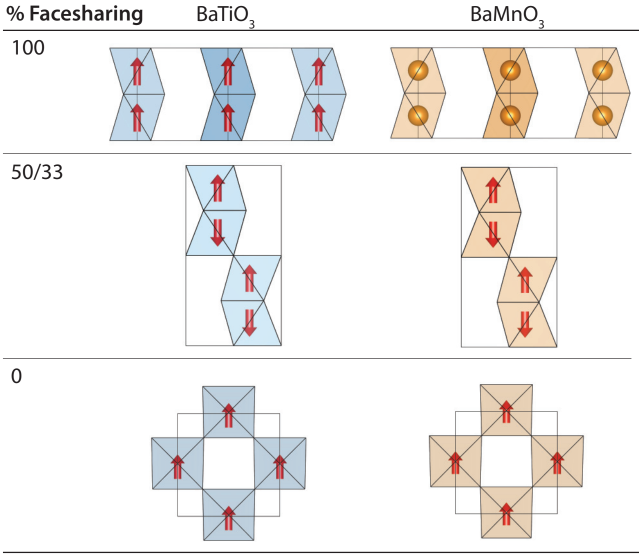

FIG. 2. Schematic illustration of polar and antipolar displacements present in various polymorphs of BaTiO$_3$ and BaMnO$_3$. The 100% facesharing polymorph of BaMnO$_3$ in this study does not have polar displacments.

for both compounds. In agreement with experiment, we find that the lowest energy structure explored for BaTiO$_3$ consists of fully corner-connected TiO$_6$ octahedra (0% facesharing). Although the experimental BaTiO$_3$ ground-state structure exhibits rhombohedral symmetry with 0% facesharing owing to polar displacements along the threefold axis [47], we consider here only the orthorhombic symmetry for simplicity. (Our calculated rhombohedral BaTiO$_3$ structure is ≈11 meV/atom lower in energy than the orthorhombic phase.) The calculated BaMnO$_3$ ground-state structure exhibits 100% MnO$_6$ facesharing connectivity, consistent with experiment [40].

Metastable phases are also observed experimentally and are realized in the laboratory by changing the synthetic process: BaTiO$_3$ will adopt a 33% facesharing hexagonal structure at very high temperature (1853 K) [50,51], and BaMnO$_3$ can be synthesized in the 50% facesharing structure through solid-state reactions [41]. The observed stability of these metastable structures is also consistent with our calculations. The 33% facesharing structure of BaTiO$_3$ is only 9 meV/atom above the orthorhombic phase. The 50% facesharing structure BaMnO$_3$ is ≈25 meV/atom higher in energy than the 100% phase; experimentally oxygen vacancies are reported to stabilize this phase [41], and they are not included in our calculations. Strong anharmonic vibrations could also play a role in stabilizing these metastable phases [52]. A thorough mapping of potential hopping barriers between local minima in the potential energy surface is left for future study.

B. Mechanical properties

Elastic material properties govern how a materials deforms linearly under an applied stresses. Hidden in this constitutive relationship is information about the bonding interactions between atoms and the anisotropy in the related forces. To that end, dynamic structural stability and transport property tensors, which are linked through electron-phonon coupling [53], are influenced by variations in the elastic constants and understanding them is useful for controlling thermomechanical and thermoelectrical responses.

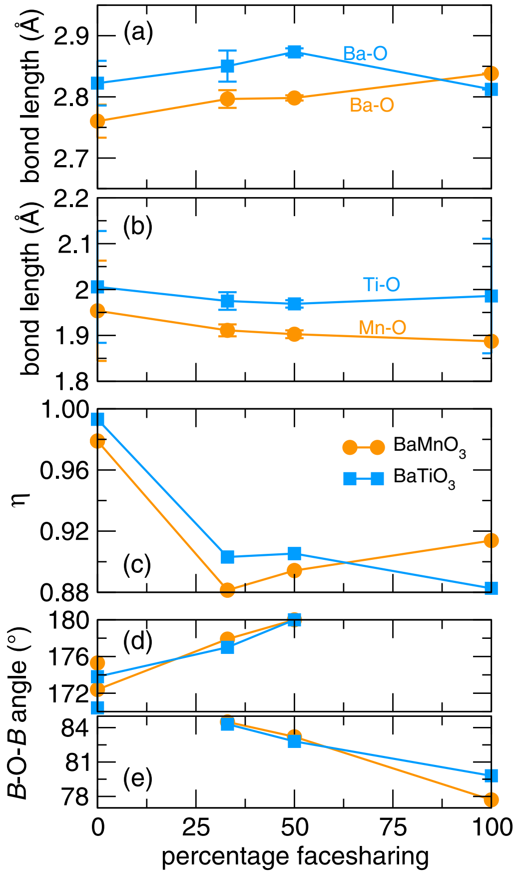

FIG. 3. Average (a) A-O and (b) B-O bond lengths in BaTiO$_3$ and BaMnO$_3$ as a function of percentage facesharing with their standard deviations. (c) shows the trigonal octahedral strain $\eta = \ell_1/\ell_2$ as defined in Fig. 1. (d) and (e) show the evolution in the metal-oxygen-metal bond angles for the corner-connected and faceshared octahedra, respectively, with percentage facesharing.

Figure 5 presents the dependencies of the bulk moduli, K, and the elastic stiffness coefficients C_{ij} with percentage facesharing for BaTiO$_3$ and BaMnO$_3$. For hexagonal crystals, there are five independent elastic constants, while orthorhombic crystals exhibit nine independent coefficients [54]. The bulk modulus is obtained from the calculated stiffness

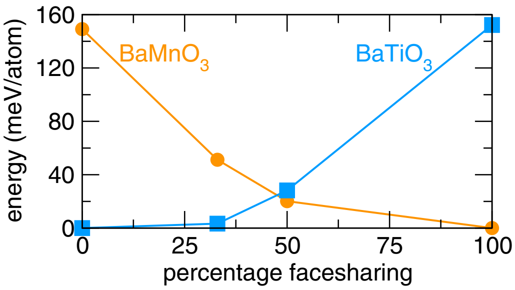

FIG. 4. Relative energy differences with percentage facesharing given with respect to the lowest energy polymorph of BaTiO$_3$ and BaMnO$_3$, respectively.

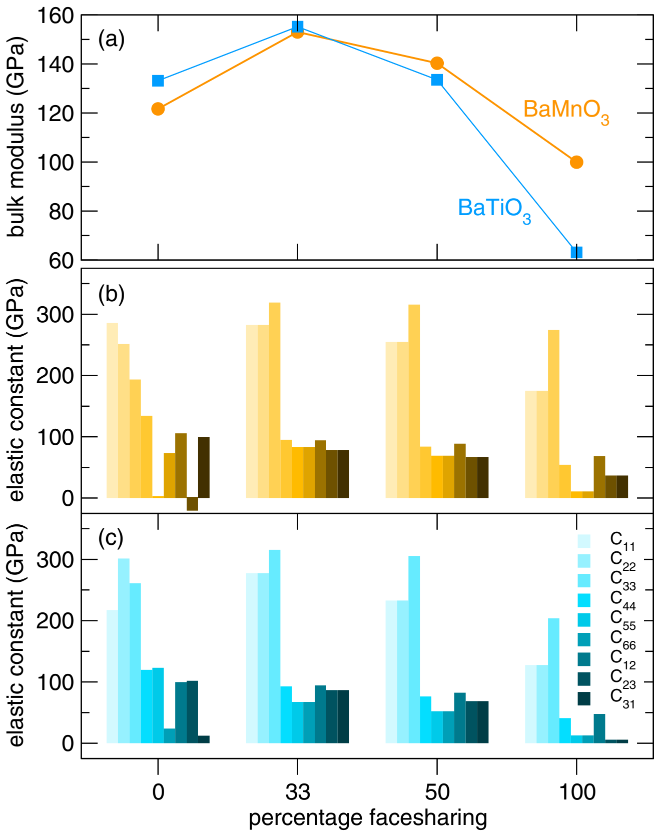

FIG. 5. Evolution in the (a) computed bulk moduli with percentage facesharing. Variation in elastic constants with percentage facesharing for (b) $BaMnO_3$ and (c) $BaTiO_3$. In these panels, each elastic stiffness coefficient at a fixed facesharing percentage is represented as a bar and the corresponding index of the tensor from left to right is 11 → 22 → 33 → 44 → 55 → 66 → 12 → 23 → 31 as shown in the legend of (c).

coefficients through a Voigt average [44] as

$$9K = (C_{11} + C_{22} + C_{33}) + 2 \times (C_{12} + C_{13} + C_{23}) .$$

Using these stiffness coefficients, we also assessed the mechanical stability of the $BaMnO_3$ and $BaTiO_3$ polymorphs using the Born elastic stability conditions [55] and find the conditions are fulfilled for all structures.[1]

We find that K and all elastic constants first increase relative to the cubic perovskite polymorphs and then decrease as facesharing percentage increases beyond 33% for both $BaTiO_3$ and $BaMnO_3$. One might expect that increasing the number of shared oxygen between adjacent (linked) BO_6 octahedra should increase the rigidity of the lattice through the removal of rotational degrees of freedom for the octahedra. That is, the topology change of the bond network should constrain the B-O-B bond angles connecting BO_6 octahedra more so than in the 0% polymorphs, which are free to bend. This effect holds whether the ions are kept frozen in the elastic constant calculation or allowed to relax as long as the topology does not drastically change, i.e., a facesharing to edgesharing, or vice versa, transformation. The elastic constant relating an axial stress and strain along the chain length, ϵ_{33}, for example, should increase K and reduce the compressibility of the material. This supposition holds when comparing the 0% and 33% polymorphs. In addition, we find the C_{33} elastic constant is indeed larger relative to other constants in the hexagonal polymorphs, reflecting the facesharing character along the z direction.

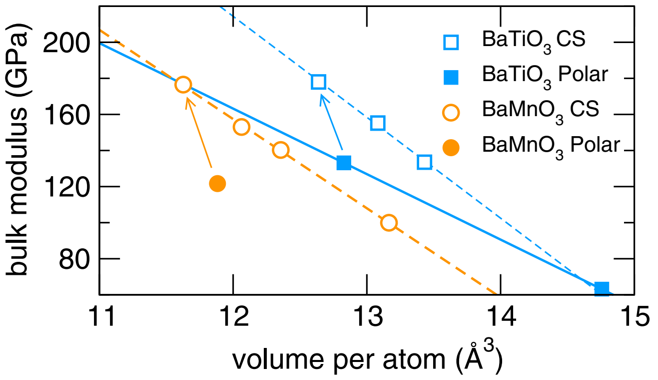

FIG. 6. Evolution in the bulk modulus with unit-cell volume per atom for centrosymmetric (CS, empty symbols) and polar perovskite polymorphs (filled symbols). The unit cell volume per atom increases with increasing percentage facesharing (from left to right). The 0% facesharing structures (solid symbols) exhibit the smallest volumes per atom and are mechanically softer owing to the polar transition metal displacements present in the structures. The arrowed open symbols are for a reference CS cubic phase and illustrate the sensitivity of the modulus to both the higher density and presence of inversion symmetry.

Consistent with other studies [56,57], we find K to decrease with increasing volume per atom (Fig. 6). The majority of this volume change is driven by the expansion of the AO_{12} dodecahedra (see inset in Fig. 5). The volumes of these dodecahedra are larger in $BaTiO_3$ than $BaMnO_3$ due to the larger ionic radius of Ti^{4+} (0.61 Å for Ti^{4+} versus 0.53 Å for Mn^{4+}) [58], which results in a larger overall volume per atom for $BaTiO_3$ than $BaMnO_3$.

The change in modulus between the 50% facesharing and 100% structures is larger for $BaTiO_3$ than $BaMnO_3$. We ascribe two reasons for this effect. There is a larger percent difference in volume per atom between the 50% facesharing and 100% structures than in $BaMnO_3$. The volume typically increases with the occurrence of polar distortions, such as the ones present in 100% facesharing $BaTiO_3$, because the soft modes have negative grüneisen parameters; when these modes are stabilized by coupling to one or more acoustic modes, the volume increases because the volume change must be positive. Additionally, only $BaTiO_3$ has a polar point group at 100% facesharing due to Ti and oxygen displacements that produce a net electric polarization. Polar distortions are intricately linked to the elastic properties of a material [59], and polar phases of $PbTiO_3$, $BaTiO_3$, and $KNbO_3$ are known

---

[1] Four relations must hold for mechanically stable hexagonal structures: $C_{11} > |C_{12}|$, $2C_{13}^2 < C_{33}(C_{11}+C_{12})$, $C_{44} > 0$, and $C_{66} > 0$, whereas for orthorhombic structures, there are six, $C_{11} > 0$, $C_{11}C_{22} > C_{22}^2$, $C_{11}C_{22}C_{33} + 2C_{12}C_{13}C_{23} - C_{11}C_{23}^2 - C_{22}C_{13}^2 - C_{33}C_{12}^2 > 0$, $C_{44} > 0$, $C_{55} > 0$, and $C_{66} > 0$.

to have reduced bulk moduli compared to centrosymmetric phases [60,61]. Lines and Glass in Ref. [59] note that the direct coupling between optical soft modes and the acoustic modes gives rise to variations in the elastic constants with temperature on passing through the transition temperature. To the extent of our knowledge, however, there does not seem to be an accepted explanation for why the elastic constants (and therefore bulk modulus) would be different between the centrosymmetric and polar phases far away from the Curie temperature. The observed increase in volume per atom across the symmetry lowering transition could account for the lower bulk modulus in the viewpoint of Anderson and Nafe [57]. However, Fischer, Wang, and Karato [62] show the change in bulk modulus in $BaTiO_3$ upon going from the cubic to tetragonal phases is anomalous even for the observed change in volume. Similarly, antiferroelectric $PbZrO_3$ exhibits softening between the cubic and antipolar orthorhombic phases, while its polar rhombohedral phase is comparable in stiffness to the orthorhombic structure [63,64]. The previously computed similarity in bulk modulus between the antipolar and polar phases of $PbZrO_3$ is not directly expected here, because the authors of that study [63] fixed the specific volumes of the two phases to be equal. The correlation between bulk modulus (lattice stiffening/softening) and (anti)polar distortions merits more attention in a broader family of (anti)ferroelectrics beyond this titanate system.

In summary, the nonmonotonic change in the mechanical properties is due to a tradeoff between the aforementioned reduction in rotational degrees of freedom for the octahedra, the polar distortions of the 0% facesharing structures, and a combination of bond length changes: shortening of BO_6 octahedral bond lengths and a lengthening of the A-O distances within the AO_n coordination polyhedron serve to decrease the atomic density (Fig. 6).

C. Electronic structure

Here we explore how changes in octahedral connectivity, i.e., different percentages of facesharing, alter the electronic properties of $BaMnO_3$ and $BaTiO_3$ at fixed chemical composition. We first examine how the relative energies of these states evolve as a function of the trigonal distortion using a point-charge model. Then we present DFT calculations, which include the complete crystal structure details and orbital hybridizations, to assess the effects that covalency have on the changes in electronic structure with the percentage of octahedral facesharing.

Figure 7 shows the splitting of the five transition metal d orbitals with changes in the trigonal angular distortion θ. In the absence of a trigonal distortion (ideal octahedra), $\theta = \arccos(1/\sqrt{3}) = 0.955 \approx 54.74^\circ$ (broken vertical line, Fig. 7), the a_{1g} orbital is lower in energy than the slightly higher energy doubly degenerate e_g^π orbitals. The e_g^σ orbitals are highest in energy. In this regard, the electronic structure of facesharing perovskites differs from that of cubic perovskites: The $t_{2g} \approx a_{1g} + e_g^\pi$ states are split by neighboring metal atoms even for undistorted octahedra.

The main energy differences among these states are given by Δ_1, corresponding to the energy difference between the a_{1g} singlet state and the e_g^π doublet while Δ_2 is the energy difference between the a_{1g} singlet state and the e_g^σ doublet as shown schematically in Fig. 1. Compression of the BO_6 octahedra corresponds to values of $\theta > 54.72^\circ$. Δ_2 is generally much larger than Δ_1 as indicated by the relative energy scales of the e_g^σ and e_g^π levels compared to the a_{1g}. As the trigonal distortion angle increases, Δ_1 approaches 0 and then becomes positive due to the a_{1g} orbital, which is oriented along the metal atom chain, experiencing stronger electronic repulsion. The dispersion of the e_g^π orbitals is reduced in comparison with the a_{1g} due to its orientation primarily in the ab plane. Based on this model, we anticipate a distortion which causes an increase in the trigonal angular distortion (compression of the octahedra) to reduce the band gap of a d^1 or d^2 transition metal compound.

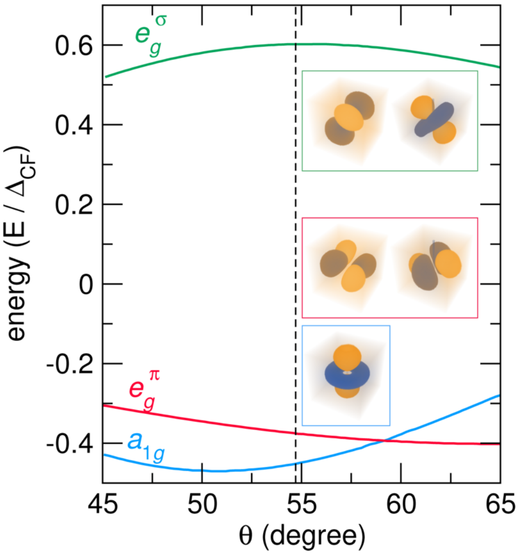

FIG. 7. Orbital energies as a function of trigonal angular distortion θ from a point charge model. Ideal octahedra exhibit $\theta \approx 54.72$ as indicated by the broken line. Values of $\theta \gtrsim 54.72$ ($\theta \lesssim 54.72$) corresponds to compression (elongation) of the octahedra along the trigonal axis. The insets depict the (upper) e_g^σ orbitals which are oriented along M-O bonds, (center) e_g^π orbitals, and (lower) a_{1g} orbital which overlaps with a similar orbital on a neighboring metal ion.

To investigate the effect of polyhedral connectivity on the electronic structure, including covalency and other features absent in the point charge model, we compute the atom resolved density of states (DOS) for all polymorphs (Fig. 8). $BaTiO_3$ with a d^0 electronic configuration exhibits a valence band primarily composed of O $2p$ states and a conduction band of Ti $3d$ character, located approximately 2 eV higher in energy at the PBEsol level. We find that increasing the percent facesharing does not significantly affect the relative energy levels or composition of the DOS (Fig. 8, left column), although the shape of the band edges do evolve. This behavior is understood as follows: The 0% and 100% facesharing structures of $BaTiO_3$ are both polar while the 33% and 50% facesharing structures are nonpolar. Polar distortions enhance the antibonding character at the Γ point by distortion of the Ti-O orbital overlap [65]. Polar distortions therefore decrease the band width [66], consistent with the decrease in band gap from 2.1 to 1.8 eV for 0%–33% facesharing followed by an increase

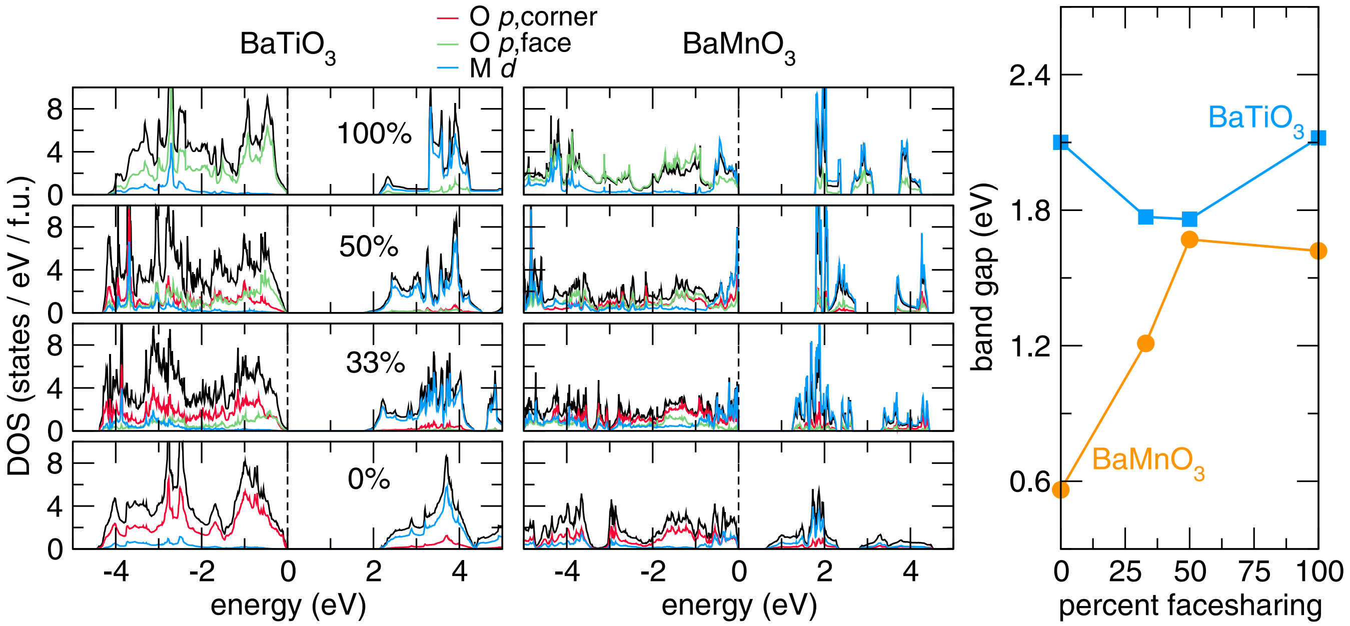

FIG. 8. Electronic density of states (DOS) for 100%, 50%, 33%, and 0% percent facesharing phases of $BaTiO_3$ (left column, descending) and $BaMnO_3$ (center column, descending). Black lines are the total DOS, red lines represent O $2p$ states from shared octahedral corners, green represents O $2p$ states from a common face, and blue represents metal $3d$ states. The minority spin channel for $BaMnO_3$ is not shown but is equivalent symmetry. (Right column) Evolution in the electronic band gaps with percentage facesharing calculated at the DFT-PBEsol level. The overall trend is that the electronic gap increases as the number of faceshared octahedra increase.

back to 2.1 eV for the 100% facesharing structure (Fig. 8, right column). In addition, there is a change from direct gap behavior for the 0% faceshared $BaTiO_3$ to indirect behavior for all polymorphs exhibiting fractional facesharedness (Table III).

In contrast, the electronic gap in d^3 $BaMnO_3$ is between the majority and minority spin Mn $3d$ states with t_{2g} (or a_{1g} and e_g^{π}) character. $BaMnO_3$ exhibits a greater degree of O $2p$ and Mn $3d$ antibonding orbital hybridization in the valence band (Fig. 8, center column). The conduction band is formed largely by the empty Mn $3d$ states with minor oxygen admixture. Across the low-energy structure, pseudo- and full gaps open with a change in percentage facesharing; for example, near 2.5 eV for the 100% faceshared structure and near −3 eV for the 0% faceshared structure. In addition, decreasing the facesharing broadens the Mn-derived conduction bandwidth centered about 2 eV, which drives a decrease in the overall charge gap (Fig. 8, right column). The band gap of $BaMnO_3$ increases from 0.56 eV in the orthorhombic structure to 1.67 eV in the 50% facesharing structure; above 50% facesharing, we find no significant change in the band gap.

To further understand the band gap dependencies with changes in percent facesharing, we next examine the electronic dispersions of the 100% facesharing $BaTiO_3$ and $BaMnO_3$ phases in more detail (Fig. 9) as they are closest in structure to the point-charge model used previously. As the point-charge model predicted, all BO_6 octahedra exhibit crystal field split $3d$ orbitals that transform as an a_{1g} singlet, e_g^{π} doublet, and higher energy e_g^{σ} doublet. The location of these states can be identified from their weak dispersion near the Fermi level. Next we use $BaTiO_3$ as an example to discern the local orbital character in the conduction band by constructing six maximally localized Wannier functions over the energy window 1 to 6 eV [45] (bands labeled $i - vi$ in Fig. 9). These six bands (including spin-degeneracy) should

TABLE III. Direct and indirect electronic band gaps for polymorphs of $BaTiO_3$ and $BaMnO_3$ at the DFT-PBEsol level obtained by assessing the band dispersion at the specified positions in the Brillouin zone (given in square brackets). Experimental values are also provided when available.

	$BaTiO_3$			$BaMnO_3$		
facesharing	Indirect	Direct	Exp[a]	Indirect	Direct	Exp
0%	2.1 [Y-Γ]	2.34 [Γ]	3.27 [67]		0.56 [T]	
33%		1.77 [Γ]	3.25 [68]	1.21 [M-Γ]	1.24 [M]	
50%		1.76 [Γ]		1.67 [H–(0.2, 0.2, 0)]	1.7 [(0.3, 0, 0)]	
100%		2.12 [Γ]		1.62 [L–A]	1.64[L]	3.2 [48]

[a] The experimental band gap of tetragonal $BaTiO_3$ is provided for the 0% facesharing category as the orthorhombic phase's gap has not been reported.

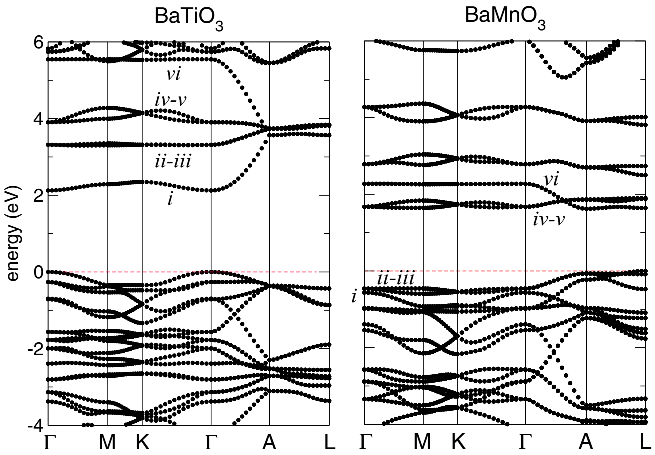

FIG. 9. Band structures of 100% facesharing BaTiO$_3$ and BaMnO$_3$. The Fermi level is set to the top of the valence band (0 eV, broken line). The majority and minority spin bands overlap in BaMnO$_3$ owing to the antiferromagnetic arrangement of spins and so only the majority spin-channel is presented. See the main text for a description of the labeled bands.

correspond to the low energy singlet and doublet; indeed, we find that the conduction band edge (band *i*) exhibits a_{1g} character (Fig. 10), consistent with our ionic description and the d^0 Ti^{4+} electronic configuration. Bands $ii - v$ exhibit e_g^π character, hence their relatively weaker dispersion from $\Gamma - A$ compared to band *i*. Band *vi* exhibits similar dispersion to band *i*.

Interestingly, the Wannier orbital for band *i* with a_{1g} character also exhibits maximal overlap with the higher energy band *vi* from $k = \Gamma(0, 0, 0) \rightarrow A(0, 0, 1/2)$ (Fig. 10). We understand this behavior as a consequence of band folding. The two Ti atoms in the $P6_3mc$ phase contribute two a_{1g} states per unit cell. The metal-metal interactions enabled by the 100% facesharing structure allow for formation of a *d*-*d* molecular orbital with bonding and antibonding (*) character. These MOs can be used to generate Bloch functions such that as one moves from $k = \Gamma(0, 0, 0) \rightarrow A(0, 0, 1/2)$, the bonding and antibonding character of the MO evolves until both states are degenerate at the *A* point [Fig. 10(b)]. By visualizing the partial charge density for both bands Fig. 10(c), we find the high energy band *vi* at approximately 5 eV is the antibonding analog of the orbital comprising the conduction band edge, band *i*. Similarly, bands *ii* and *iii* exhibit e_g^π character akin to bands *iv* and *v*, but because these orbitals point away from neighboring Ti atoms, their interaction is weaker. In BaMnO$_3$, similar dispersions are observed although the electron filling is different. The Fermi level lies between bands of e_g^π and a_{1g}^* character owing to the d^3 configuration, bands labeled *ii-iii* in the range −0.5 to 0 eV and *vi* at 1.6–2.2 eV respectively. The partial charge density is visualized in Ref. [33].

Molecular orbital theory indicates the energies of the a_{1g} and a_{1g}^* orbitals at Γ relative to their level at *A* is a function of the orbital overlap between neighboring Ti atoms in BaTiO$_3$. Therefore the energy-level splitting of the a_{1g} bonding-antibonding states at Γ should be susceptible to changes in the metal-metal distance, which are tuned at the unit cell level via the trigonal octahedral strain η. The η-induced splitting should be greater in BaTiO$_3$, because these metal-derived MOs form the conduction band edge, with perturbations apparent in the electronic band gap, whereas BaMnO$_3$ exhibits e_g^π and e_g^σ orbital character at the band edges. This η-induced splitting is a key aspect of the physics missing from the point charge model due to its neglect of covalency. Experimentally, trigonal distortions can be modulated with pressure [69] or in epitaxial films of complex oxides [18,70], offering an added control knob for electronic structure control in facesharing perovskite polymorphs.

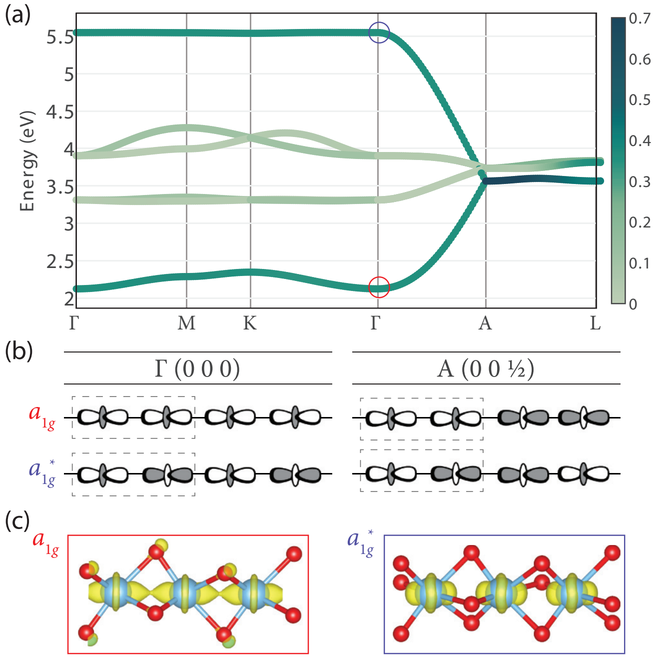

FIG. 10. (a) Projection of the Wannier orbital with a_{1g} character onto the manifold of conduction band states. (b) Schematic a_{1g} bonding and a_{1g}^* antibonding orbital combinations at the Γ and A points illustrate why the bonding (antibonding) bands run "uphill" ("downhill") along the trajectory Γ → A. The band degeneracy at the A point is due to the equal proportion of mixed-bonding character. (c) The DFT partial charge density, supporting the assignment of the bonding and antibonding character at the zone center, derived from the metal-metal bonding with a_{1g} and a_{1g}^* symmetry. The isosurface levels for the density contours correspond to $0.128\,e\,\text{Å}^{-3}$ and $0.162\,e\,\text{Å}^{-3}$, respectively.

We assess this hypothesis by computing the electronic band gaps for the 100% facesharing BaTiO$_3$ and BaMnO$_3$ phases after applying uniaxial tension and compression to the octahedra, modifying η, via shortening of the *c* axis by up to ±0.44 Å and allowing the ions and transverse lattice parameters to fully relax under the mechanical constraints (Fig. 11). For BaTiO$_3$, as the octahedra stretch (compress), the bands at 2 and 5 eV in the conduction band manifold move closer together (further apart), which increases (decreases) the band gap. This suggests that coherent strain could be used to control the $B_1\,d - B_2\,d$ overlap in d^0 hexagonal polymorphs through epitaxial boundary conditions, i.e., clamping the in-plane lattice constants to achieve a desired trigonal distortion along the out-of-plane direction. Between η values of 0.868 and 0.900, corresponding to 2.15% tensile and −2.15% compressive coherent uniaxial strains, the band gap shrinks from

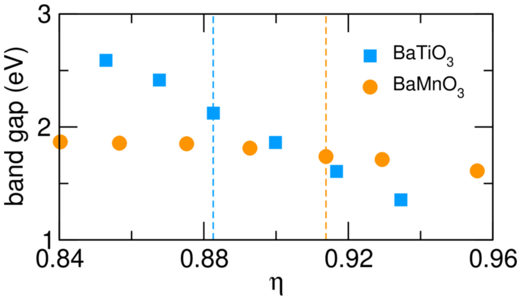

FIG. 11. Evolution in the electronic band gap for the 100% facesharing BaTiO$_3$ and BaMnO$_3$ phases with respect to uniaxial tension and compression. The mechanical constraints induce trigonal octahedral strains, η, that alter the transition metal distances and thus the $d-d$ interactions. The band gap of BaTiO$_3$ is more strongly affected than that of BaMnO$_3$ because of the a_{1g} character at the conduction band edge. The equilibrium trigonal octahedral strains for BaTiO$_3$ and BaMnO$_3$ are indicated by the broken vertical lines.

2.42 to 1.86 eV, a 560-meV decrease. The hexagonal structure with faceshared octahedra uniquely enables this interaction as facesharing requires the Ti cations be closer together. This direct metal-metal interaction is missing from our ionic model, and hence explains why the model in Fig. 7 predicts the a_{1g} should rise in energy with compression rather decrease with compression as found in the DFT calculations.

In BaMnO$_3$, the effect of the trigonal distortion on the band gap is much weaker (Fig. 11), because the band edges are primarily of e_g^π character. Between η values of 0.893 and 0.929, corresponding to 2.45% tensile and −1.77% compressive uniaxial strains, the band gap decreases 100 meV from 1.81 to 1.71 eV. For comparison, prior work on uniaxial strain in 0% facesharing tetragonal perovskite LaMnO$_3$ showed a 543 meV decrease in band gap between −2% compressive and 2% tensile strain. The e_g^π orbitals are primarily oriented in the xy plane orthogonal to the direction of the applied strain; consequently, the dependence of their energy levels on the Mn-Mn distances along the z direction are reduced.

The trigonal distortions alone cannot explain the difference in band-gap evolution with facesharing between BaTiO$_3$ and BaMnO$_3$. Examining the orbital overlaps in the projected DOS (Fig. 8), it is clear that there is a large degree of metal-oxygen (M-O) covalent interactions in BaMnO$_3$ as others have noted [23]. Covalency appears to increase in BaMnO$_3$, where the local magnetic moment on Mn is 2.42, 2.34, 2.37, and 2.28 μ_β in the 0, 33, 50, and 100% facesharing variants, respectively. It is also clear that M-O covalency is lower in the 100% facesharing BaTiO$_3$ variant. Therefore one would reasonably expect that the ≈9% increase in the MnO$_6$ octahedra size from 100% to 0% facesharing would shift the energy of the conduction band manifold more than the BaTiO$_3$ conduction manifold with the reduced orbital hybridization. Thus, while d^0 cations might be expected to be the most susceptible to band engineering via trigonal distortions, it is d^n configurations that appear to be most affected by the change in cation environment across various levels of facesharing. However, since the polymorphs with intermediate levels of facesharing exhibit an orbital structure combining features of cubic perovskites with those of the 100% hexagonal facesharing variant, further assessments are required to quantitatively determine all of the atomic scale structure features controlling the band edges.

IV. CONCLUSIONS

Our study is one of the first to quantify and describe the key interactions governing the elastic and electronic properties of perovskite oxides with faceshared octahedra. We assessed the dependencies of the bulk moduli and band gap on the percentage of facesharing using electronic structure calculations on BaTiO$_3$ and BaMnO$_3$. We found that increased facesharing reduces the stiffness of the lattice through decreased atomic density and polar distortions. Although the relative orbital energy levels in d^0 BaTiO$_3$ are weakly affected by changes in the percentage facesharing, we found that the Kohn-Sham gap at the DFT-PBEsol level of d^3 BaMnO$_3$ increases from 0.6 eV (0% facesharing) to 1.6 eV (100% facesharing). In addition, we examined the role of covalent metal-metal interactions and found that they are necessary to explain changes in the electronic structure induced by trigonal distortions. These trigonal distortions enable structural access to the electronic bandgaps via changes in the a_{1g} overlap. Our work is by no means an exhaustive search for the best potential materials to study with facesharing structures. We hope future efforts might exploit the degrees of freedom active with facesharing and described here to control Jahn-Teller distortions in systems that should have orbital degeneracies, explore spin-orbit effects in 3d to 5d transition metal compounds, or achieve novel magnetic orders in multi cation compounds such as those with d^0-d^7 or d^3-d^5 configurations. This study motivates the search for structural descriptors of other properties in these oxides and experimental investigations focused on stabilizing other transition metal cations in hexagonal perovskite polymorphs.

ACKNOWLEDGMENTS

The authors would like to thank Nenian Charles and Danilo Puggioni for many enlightening discussions. Funding for this work came from NSF DMR-1729303. Calculations were performed using the QUEST HPC facility at Northwestern, the HPC facility at the Extreme Science and Engineering Discovery Environment (NSF, ACI-1548562), and the CARBON cluster at Argonne National Laboratory. Use of the Center for Nanoscale Materials, an Office of Science user facility, was supported by the U.S. Department of Energy, Office of Science, Office of Basic Energy Sciences, under Contract No. DE-AC02-06CH11357.

---

[1] J. M. Rondinelli, S. J. May, and J. W. Freeland, MRS Bull. **37**, 261 (2012).

[2] M. A. Green, A. Ho-Baillie, and H. J. Snaith, Nat. Photonics **8**, 506 (2014).

[3] S. Ghosh, D. Di Sante, and A. Stroppa, J. Phys. Chem. Lett. **6**, 4553 (2015).
[4] J. Suntivich, K. J. May, H. A. Gasteiger, J. B. Goodenough, and Y. Shao-Horn, Science **334**, 1383 (2011).
[5] H. Y. Hwang, S.-W. Cheong, P. G. Radaelli, M. Marezio, and B. Batlogg, Phys. Rev. Lett. **75**, 914 (1995).
[6] L. M. Rodriguez-Martinez and J. P. Attfield, Phys. Rev. B **54**, R15622 (1996).
[7] Y. Moritomo, H. Kuwahara, Y. Tomioka, and Y. Tokura, Phys. Rev. B **55**, 7549 (1997).
[8] D. G. Schlom, L.-Q. Chen, C.-B. Eom, K. M. Rabe, S. K. Streiffer, and J.-M. Triscone, Annu. Rev. Mater. Res. **37**, 589 (2007).
[9] S. Stemmer and A. J. Millis, MRS Bull. **38**, 1032 (2013).
[10] I. E. Castelli, M. Pandey, K. S. Thygesen, and K. W. Jacobsen, Phys. Rev. B **91**, 165309 (2015).
[11] A. Galdi, C. Sacco, P. Orgiani, F. Romeo, and L. Maritato, J. Cryst. Growth **459**, 56 (2017).
[12] P. Moetakef, C. A. Jackson, J. Hwang, L. Balents, S. J. Allen, and S. Stemmer, Phys. Rev. B **86**, 201102(R) (2012).
[13] E. J. Moon, P. V. Balachandran, B. J. Kirby, D. J. Keavney, R. J. Sichel-Tissot, C. M. Schlepütz, E. Karapetrova, X. M. Cheng, J. M. Rondinelli, and S. J. May, Nano Lett. **14**, 2509 (2014).
[14] J. Chakhalian, J. W. Freeland, A. J. Millis, C. Panagopoulos, and J. M. Rondinelli, Rev. Mod. Phys. **86**, 1189 (2014).
[15] X. Liu, S. Middey, Y. Cao, M. Kareev, and J. Chakhalian, MRS Commun. **6**, 133 (2016).
[16] Z. Liao, M. Huijben, Z. Zhong, N. Gauquelin, S. Macke, R. J. Green, S. Van Aert, J. Verbeeck, G. Van Tendeloo, K. Held, G. A. Sawatzky, G. Koster, and G. Rijnders, Nat. Mater. **15**, 425 (2016).
[17] D. Kan, R. Aso, R. Sato, M. Haruta, H. Kurata, and Y. Shimakawa, Nat. Mater. **15**, 432 (2016).
[18] I. Hallsteinsen, J. E. Boschker, M. Nord, S. Lee, M. Rzchowski, P. E. Vullum, J. K. Grepstad, R. Holmestad, C. B. Eom, and T. Tybell, J. Appl. Phys. **113**, 183512 (2013).
[19] I. Hallsteinsen, E. Folven, F. K. Olsen, R. V. Chopdekar, M. S. Rzchowski, C. B. Eom, J. K. Grepstad, and T. Tybell, APL Mater. **3**, 062501 (2015).
[20] A. Abakumov, A. Tsirlin, and E. Antipov, in *Comprehensive Inorganic Chemistry II*, edited by J. Reedijk and K. Poeppelmeier (Elsevier, Amsterdam, 2013), Chap. 2.01, pp. 1–40.
[21] D. I. Khomskii, K. I. Kugel, A. O. Sboychakov, and S. V. Streltsov, J. Exp. Theor. Phys. **122**, 484 (2016).
[22] M. B. Nielsen, D. Ceresoli, P. Parisiades, V. B. Prakapenka, T. Yu, Y. Wang, and M. Bremholm, Phys. Rev. B **90**, 214101 (2014).
[23] R. Søndenå, S. Stølen, P. Ravindran, T. Grande, and N. L. Allan, Phys. Rev. B **75**, 184105 (2007).
[24] V. M. Goldschmidt, Naturwissenschaften **14**, 477 (1926).
[25] I. Terasaki, S. Ito, T. Igarashi, S. Asai, H. Taniguchi, R. Okazaki, Y. Yasui, K. Kobayashi, R. Kumai, H. Nakao, and Y. Murakami, Crystals **6**, 27 (2016).
[26] S. Kanungo, R. Datta, S. K. Panda, and T. Saha-Dasgupta, J. Phys.: Condens. Matter **25**, 505503 (2013).
[27] N. V. Tarakina, A. P. Tyutyunnik, G. V. Bazuev, A. D. Vasilev, C. Gould, I. V. Nikolaenko, and I. F. Berger, Dalton Trans. **44**, 18527 (2015).
[28] J. T. Rijssenbeek, R. Jin, Y. Zadorozhny, Y. Liu, B. Batlogg, and R. J. Cava, Phys. Rev. B **59**, 4561 (1999).
[29] S. Stølen, E. Bakken, and C. E. Mohn, Phys. Chem. Chem. Phys. : PCCP **8**, 429 (2006).
[30] R. Seshadri and R. Basu, Periodic Table of Effective Ionic Radii (2002).
[31] Wolfram Research Inc., MATHEMATICA, Version 11.0.1 (2016).
[32] https://github.com/MTD-group/PolyhedralConnectivity Supplement.
[33] See Supplemental Material at http://link.aps.org/supplemental/10.1103/PhysRevB.100.064101 for additional structure information.
[34] J. P. Perdew, A. Ruzsinszky, G. I. Csonka, O. A. Vydrov, G. E. Scuseria, L. A. Constantin, X. Zhou, and K. Burke, Phys. Rev. Lett. **100**, 136406 (2008).
[35] G. Kresse and J. Furthmüller, Comput. Mater. Sci. **6**, 15 (1996).
[36] G. Kresse and J. Furthmüller, Phys. Rev. B **54**, 11169 (1996).
[37] G. Kresse, Phys. Rev. B **59**, 1758 (1999).
[38] P. E. Blöchl, Phys. Rev. B **50**, 17953 (1994); J. Lehtomki, I. Makkonen, M. A. Caro, A. Harju, and O. Lopez-Acevedo, J. Chem. Phys. **141**, 234102 (2014).
[39] S. L. Dudarev, G. A. Botton, S. Y. Savrasov, C. J. Humphreys, and A. P. Sutton, Phys. Rev. B **57**, 1505 (1998).
[40] E. J. Cussen and P. D. Battle, Chem. Mater. **12**, 831 (2000).
[41] J. J. Adkin and M. A. Hayward, J. Solid State Chem. **179**, 70 (2006).
[42] Y. Le Page and P. Saxe, Phys. Rev. B **65**, 104104 (2002).
[43] D. R. Hamann, K. M. Rabe, and D. Vanderbilt, Phys. Rev. B **72**, 033102 (2005).
[44] R. Hill, Proc. Phys. Soc. London, Sect. A **65**, 349 (1952).
[45] A. A. Mostofi, J. R. Yates, Y.-S. Lee, I. Souza, D. Vanderbilt, and N. Marzari, Comput. Phys. Commun. **178**, 685 (2008).
[46] K. W. Kirby and B. A. Wechsler, J. Am. Ceram. Soc. **74**, 1841 (1991).
[47] G. H. Kwei, A. C. Lawson, S. J. L. Billinge, and S. W. Cheong, J. Phys. Chem. **97**, 2368 (1993).
[48] T. N. Stanislavchuk, A. P. Litvinchuk, R. Hu, Y. H. Jeon, S. D. Ji, S.-W. Cheong, and A. A. Sirenko, Phys. Rev. B **92**, 134308 (2015).
[49] R. Søndenå, P. Ravindran, S. Stølen, T. Grande, and M. Hanfland, Phys. Rev. B **74**, 144102 (2006).
[50] J. Akimoto, Y. Gotoh, and Y. Oosawa, Acta Crystallogr. Sect. C **50**, 160 (1994).
[51] X. Lu and Z. Jin, Calphad **24**, 319 (2000).
[52] J. Klarbring and S. I. Simak, Phys. Rev. B **97**, 024108 (2018).
[53] R. Escamilla, M. Romero, and F. Morales, Solid State Commun. **152**, 249 (2012).
[54] D. C. Wallace, *Solid State Physics* (Academic Press, New York, 1970), Vol. 25, pp. 301–404.
[55] F. Mouhat and F.-X. Coudert, Phys. Rev. B **90**, 224104 (2014).
[56] M. de Jong, W. Chen, R. Notestine, K. Persson, G. Ceder, A. Jain, M. Asta, and A. Gamst, Sci. Rep. **6**, 34256 (2016).
[57] O. L. Anderson and J. E. Nafe, J. Geophys. Res. **70**, 3951 (1965).
[58] R. D. Shannon, Acta Crystallogr. Sect. A **32**, 751 (1976).
[59] M. E. Lines and A. M. Glass, *Principles and Applications of Ferroelectrics and Related Materials* (Oxford University Press, Oxford, 2001), pp. 334–370.

[60] S. F. Yuk, K. C. Pitike, S. M. Nakhmanson, M. Eisenbach, Y. W. Li, and V. R. Cooper, Sci. Rep. **7**, 43482 (2017).

[61] J. J. Wang, F. Y. Meng, X. Q. Ma, M. X. Xu, and L. Q. Chen, J. Appl. Phys. **108**, 034107 (2010).

[62] G. J. Fischer, Z. Wang, and S.-i. Karato, Phys. Chem. Miner. **20**, 97 (1993).

[63] R. Kagimura and D. J. Singh, Phys. Rev. B **77**, 104113 (2008).

[64] M. Rashid, Q. Mahmood, F. Babar, S. M. Ramay, and A. Mahmood, Mater. Res. Express **6**, 066311 (2019).

[65] H. W. Eng, P. W. Barnes, B. M. Auer, and P. M. Woodward, J. Solid State Chem. **175**, 94 (2003).

[66] F. Wang, I. Grinberg, and A. M. Rappe, Appl. Phys. Lett. **104**, 152903 (2014).

[67] S. H. Wemple, Phys. Rev. B **2**, 2679 (1970).

[68] Y. Akishige, J. Phys. Soc. Jpn. **64**, 4033 (1995).

[69] Y. Zhao, W. Yang, N. Li, Y. Li, R. Tang, H. Li, H. Zhu, P. Zhu, and X. Wang, J. Phys. Chem. C **120**, 9436 (2016).

[70] K. Inumaru, K. Baba, and S. Yamanaka, Phys. Rev. B **73**, 052504 (2006).